Manipulating the Diffusion Energy Barrier at the Lithium Metal Electrolyte Interface for Dendrite-free Long-life Batteries

Jyotshna Pokharel
South Dakota State University
Arthur Cresce
U.S. Army Research Laboratory https://orcid.org/0000-0002-3894-6083
Bharat Pant
University of Texas at Arlington
Ashim Gurung
South Dakota State University
Wei He
South Dakota State University
Abiral Baniya
South Dakota State University
Buddhi Lamsal
South Dakota State University
Zhongjiu Yang
South Dakota State University
Stephen Gent
South Dakota State University
Ye Cao
The University of Texas at Arlington https://orcid.org/0000-0002-7365-7447
William Goddard III
California Institute of Technology
Kang Xu (✉ conrad.k.xu.civ@mail.mil)
U.S. Army Research Laboratory https://orcid.org/0000-0002-6946-8635
Yue Zhou
South Dakota State University https://orcid.org/0000-0002-5060-5054

Article

Keywords:

Posted Date: August 24th, 2022

DOI: https://doi.org/10.21203/rs.3.rs-1915687/v1

Abstract

Constructing an artificial solid electrolyte interphase (SEI) on lithium metal electrode is a promising approach to address the rampant growth of dangerous lithium morphologies (dendritic and dead Li^0) and low Coulombic efficiency that plague development of lithium metal batteries. But it is not known how the Li^+ transfer behavior in the SEI is coupled with mechanical properties. We demonstrate here a facile and scalable solution-processed approach to form a Li_3N-rich SEI with a phase-pure crystalline structure that minimizes the diffusion energy barrier of Li^+ across the SEI. Compared with a polycrystalline Li_3N SEI obtained from conventional practice, our phase-pure/single crystalline Li_3N-rich SEI constitutes an interphase of high mechanical strength and low Li^+ diffusion barrier. We elucidate the correlation among Li^+ transference number, diffusion behavior, concentration gradient, and the stability of the lithium metal electrode by integrating phase field simulations with experiments. We demonstrate extreme reversibility and ultra-stable charge/discharge cycling behaviors for both symmetric cells and full lithium-metal batteries constructed using this Li_3N-rich SEI. These studies provide new insight into the designing and engineering an ideal artificial SEI for stable and high-performance lithium metal batteries.

Introduction

The increasing high demand for rechargeable energy sources to power electronics, electric vehicles, and large-scale grid energy storage has driven rigorous research in the field of energy-dense lithium-based batteries[1, 2, 3]. To match the growing demand, development of high energy density batteries is of utmost importance. This cannot be met adequately by state-of-art lithium-ion batteries, which exhibit maximum energy densities of 300 Wh kg^{-1}[4, 5]. The metallic lithium anode has a high theoretical specific capacity (3,860 mAh g^{-1}) and a low reduction potential (-3.04 V vs standard hydrogen electrode), making it the ultimate choice of anode material for high energy Li-based rechargeable batteries[1, 6, 7, 8]. Although Li metal anodes enable realization of LIBs with high energy density, they can form dangerous lithium morphologies (dendritic and the subsequent mossy Li^0) and associated electrolyte decomposition, which eventually leads to poor reversibility, with low Coulombic efficiency (CE) and safety hazards[9]. Considerable efforts have been devoted to addressing the challenges of lithium metal anodes, including interfacial engineering[8, 10, 11, 12, 13, 14, 15], electrolyte engineering [5, 16, 17, 18, 19, 20, 21], minimizing volume change by using stable hosts[22, 23, 24, 25], and preventing dendrite propagation by use of modified separators[26, 27, 28].

Partial physical suppression of dendrite growth has been well studied in the existing literature, but in order to fully eliminate the instable interface between the Li metal electrode and electrolyte, one must understand the fundamental mechanism of dendrite growth. Formation of Li dendrites are induced by the chemical and morphological inhomogeneity of the SEI formed on the Li^0 surface formed in-situ, which leads to uneven local current density. Efforts have been made to relate dendritic Li^0 formation to the interfacial kinetics as described by Sand’s equation (Equation S1) [29, 30]or to diffusion-limited aggregation model by Chazalviel[31], but the actual factors involved are far more complicated than the diffusion models derived from metal ion deposition from aqueous electrolytes, where the interphase does not exist. Nevertheless, non-quantitative approximate relations exist between the fractal deposition pattern and the maximum interfacial current. These show that rapid consumption of Li^+ in certain locations does result in concentration polarization, which invites local enrichment of Li^+ and subsequent preferential deposition[32]. Hence, the diffusion energy barrier of Li^+ at the interface plays a critical role, while the lithium transference number, which quantifies the pure contribution from Li^+ to the entire migration flux, has a decisive impact on the manner in which Li^+ ions approach the interphase-enclosed surface of Li^0 [33]. Consequently, the most directive and effective approach to guide Li deposition in a homogenous manner so that dendrite formation is minimized is to decrease the diffusion energy barrier and increase the transference number of Li^+ ion. Most current research toward increasing transference number focuses on single-ion conducting solid polymers and their composites [34, 35]. Single ion-conducting polymers offer both a rigid framework of interconnected nanopores and a high transference number, but are limited by low mechanical strength and poor ionic conductivity[34, 35]. Recent efforts have demonstrated solid state electrolytes based on ceramics with improved transference number. However, challenges remain because the solid electrolytes need to interface intimately with the solid Li metal electrode while there are difficulties in controlling thickness, and the brittle nature of the ceramic solid electrolytes[34, 35, 36]. Hence, it is highly desired to develop a new strategy to engineer the interface between Li metal electrode and the electrolyte with both near-unity Li^+ ion transport and robust mechanical strength to enable “dual protection” for the stabilization of Li metal electrode.

Herein, we propose a rational design of an artificial SEI layer composed of tetramethylethylenediamine (TEMED) which exhibits low diffusion energy barrier, high Li^+ transference number, and unrivaled mechanical strength to simultaneously overcome diffusion and advection-limited ion transport to achieve dendrite-free Li plating/stripping. Notably, TEMED is passivated spontaneously when in contact with the metallic Li to form pure α-phase Li_3N. Differing from conventional Li_3N artificial SEI that is fabricated from the exposure of the Li chip in N_2 atmosphere, an artificial SEI achieved in this way offers excellent Li^+ ion conductivity with a lower energy barrier for Li^+ ion migration, further benefitting ion transport at the interface between electrode and electrolyte. This effectively facilitates transport of Li^+ ions across the electrode surface, leading to high transference number and excellent mechanical strength that tolerates volume change to enforce more uniform Li^+ ion flux. The TEMED treated symmetrical cell shows outstanding plating/stripping cycles with reduced overpotential and the full cell exhibits remarkably improves cycling stability and capacity retention as well as capacity utilization at high rates compared to bare Li. To our best knowledge, this is the first demonstration of Li treated with TEMED as a solution for the issues caused by Li metal anode.

Results

Preparation of an artificial SEI layer.

Lithium chips were completely immersed into a TEMED solution in a petri dish to let Li metal react with TEMED shown in Fig. 1a. A color change is observed from shiny silver to light black and later to dark black as the reaction time between the TEMED and Li metal increases. To obtain the optimum reaction time, lithium chips were dipped in the TEMED for 6 hours, 12 hours and 18 hours. The shiny silver surface of the bare Li metal changes color and covers the surface of the Li metal as the reaction time increases. Figure 1c shows that with the reaction time of 6 hours, the reacted TEMED film does not fully cover the Li surface. With 12 and 18 hours of TEMED reaction time, full coverage of the artificial SEI layer is observed. The artificial TEMED-based SEI layer at 6 hours of reaction time does not cover the surface completely as observed in visual and SEM inspection, which would allow the electrolyte to react with the Li metal directly, leading to consumption of electrolyte and Li metal resulting in low CE and capacity decay. In comparison, SEM images of the artificial SEI with treatment time of 12 and 18 hours fully covers the Li metal surface, thereby preventing direct contact of the electrolyte with Li metal. Cross-sectional SEM images (Fig. 1j-m) shows the average thickness (t) of the artificial SEI layer obtained with different TEMED treatment times. SEI layers with thickness of 5, 10, and 20 μm was obtained for 6, 12, and 18 hours respectively. It is assumed that a thicker SEI will have a higher Li-ion barrier energy and higher impedance, resulting in slower Li^+ ion diffusion. Thus, the SEI layer thickness should be optimized in order to prevent direct contact between Li metal and electrolyte while maintaining usefully high Li^+ ion conductivity.

Material characterization, electrochemical spectroscopy and transference number measurement

Figure 2

Contact angle measurement of (a) bare Li, (b) TEMED treated Li, (c) XRD spectrum for TEMED treated Li. (d) EIS measurement for bare Li and TEMED treated Li. Steady-state current under 10 mV polarization for (e) Li-Li symmetric cell (f) TEMED-Li/TEMED-Li symmetric cell. Inset shows EIS measurement before and after polarization.

Contact angle measurement have been performed to determine the wettability of the electrolyte on bare Li and TEMED treated Li in **Fig. 2 (a,b)**. To ensure good Li^+ ion conductivity, rate capability and formation of a stable SEI layer, the electrolyte must be able to significantly wet the electrode[37]. The contact angle for bare Li is 41° suggesting poor wettability with the electrolyte which could cause blocking of ionic conductivity pathways. In contrast, TEMED treated Li shows a significantly lower contact angle of 12°. This result suggests that the TEMED treated Li has better wettability and affinity with the electrolyte which is beneficial to homogenize ion distributions in the vicinity of the anode, which could support efficient Li^+ ion transport to the Li metal anode[38]. The phase changes of TEMED treated Li were characterized by X-ray diffraction (XRD) (Fig. 2c). Distinct Li metal peaks of (110), (200) and (211) were observed at 36°, 52°, and 65° [10] and Li_3N peaks of (001) and (002) at 22.96° and 46.6° respectively. In comparison, conventional methods to obtain Li_3N, where lithium chips under nitrogen flow show a polycrystalline structure with (001), (100), (002), (110) and (102) peaks for Li_3N (Supporting Information

Figure S1). These Li_3N diffraction peaks for TEMED treated Li not only indicate the formation of α-phase Li_3N but also reveal that the Li_3N film obtained from TEMED treatment is highly orientated along the direction vertical to the Li surface. α-phase Li_3N offers excellent Li^+ ion conductivity and implies a lower Li^+ migration energy barrier which further benefits ion transport at the interface between electrode and electrolyte[39].

Electrochemical Impedance Spectroscopy (EIS) measurements were performed to further study the characteristics of the electrode interface. Figure 2d shows the comparison of EIS for bare Li and for TEMED treated Li. The first semicircle in the higher frequency range indicates the interfacial resistance of the artificial SEI or resistance of Li^+ flux through an artificial SEI, while the second semicircle in the lower frequency range indicates the charge transfer resistance R_{ct} between the artificial SEI and the electrolyte. The untreated Li symmetrical cell showed a high resistance of ~ 400 ohms, whereas for the TEMED treated Li symmetric cell, we observed a reduced resistance of ~ 200 ohm. We attribute the smaller overall impedance of the TEMED treated Li cell to the Li^+ transport performance of the Li_3N layer formed at the interface. The Li^+ ion conductivity of the TEMED treated Li was calculated as ~ $4.19\text{x}10^{-1}$ mS cm^{-1} based on series resistance of the symmetric cell, a sufficiently high value to establish a fast Li^+ ion exchange channel between Li metal and electrolyte[10].

The transference number of Li^+ ion at the interface between the Li metal electrode and the electrolyte was characterized to study the effect of Li^+ ion transport on stabilization of the Li metal electrode. High cation transference number are desirable to avoid concentration gradients in the cell and to delay the nucleation and growth of lithium metal dendrites while charging the cell. It should be noted that use of a conventional organic carbonate liquid electrolyte is not recommended for Li metal battery cells. In a typical organic carbonate liquid electrolyte with binary lithium salt, the transference number t^+ is between 0.1 and 0.4[40]. Higher t^+ can be obtained in polymeric, ceramic, or nanoparticle-based electrolytes, in which the anions are immobilized to a stationary or slow-moving support. However, these materials exhibit low ionic conductivity and are applicable only where elevated temperature are applied. We expect that the lithium nitride layer with a pure α-phase on top of lithium metal will confine the liquid electrolytes to the 3D network in the SEI layer. We determined the transference numbers in a Li-Li and TEMED Li-TEMED Li symmetric cells. The cell was initially conditioned to establish a stable interface. For this we performed charge and discharge cycles at 0.01 mA cm^{-2}, with 4 hour charge, 30 minute rest and 4 hour discharge, with the process repeated 6 times. The cell was then polarized at 10 mV for 10 hours to ensure steady state (Fig. 2e,**f**). EIS spectra before polarization and after the steady-state had been reached is shown in inset of **Fig. 2e,f**. The steady state cation transference number was then calculated using the Bruce-Vincent Eq. (1).

$$t^+= \frac{I_s(\Delta V - I_o R_o)}{I_o(\Delta V - I_s R_s)} \quad (1)$$

where t^+ is the steady-state cation transference number, ΔV is the applied voltage, I_o is the initial current, I_S is the steady-state current, R_o is the initial interfacial resistance, R_S and is the steady-state interfacial resistance. The calculated result shows that the TEMED treated Li electrode exhibits a high steady-state cation transference number of $t^+ = 0.668$, which can be compared to the bare Li with $t^+ = 0.37$ in the bulk electrolyte. This result strengthens our understanding that the TEMED treated Li metal/electrolyte interphase plays a dominant role in altering Li^+ transport behavior. The improvement in the cation transference number with the artificial SEI layer has the potential to eliminate dendrite growth by lowering the diffusion energy barrier and regulating the ion concentration at the interface in organic electrolyte rather than solid-state electrolyte.

Phase field Simulation

Figure 3. Phase-field simulation of Li dendrite growth from bare Li anode and from Li anode covered with Li_3N protective layer of high Li ion diffusivity. (a) Dendrite morphology grown on bare lithium metal represented by phase-field variable ξ. (b) Dendrite morphology grown on lithium metal having high diffusivity protective layer made of Li_3N. (c) Concentration profile of Li^+ ion across the x-axis along the tip of the dendrite for bare lithium. The image on the inset shows the concentration of Li^+ ion across the battery. (d) Li^+ ion concentration profile along the tip of dendrite for lithium having high diffusivity Li_3N layer. (e) Electric field profile along the tip of dendrite for bare lithium. The image on the inset shows the 2D distribution of the electric field. (f) Electric field profile along the tip of the dendrite for lithium having high diffusive Li_3N layer.

The Arrhenius Equation (Supplementary Information Eq. 2) indicates that a decrease in the activation energy leads a increase in the diffusion coefficient. This decrease in activation energy for diffusion lowers Li^+ migration energy barriers which increases ion transport at the interface between the electrode and electrolyte. The transference number relates the diffusion of Li^+ ion and its counterion as $t^+ = \frac{D_+}{D_- + D_+}$ [34], where D_+ is the Li^+ ion diffusion coefficient and D_- is anion diffusion coefficient. This relation shows that effective transport of Li^+ across the electrode surface results in a higher transference number than that observed in the liquid electrolyte. Comparative Arrhenius-plots for TEMED treated Li and bare Li are shown in Figure S2. Bare Li showed an activation energy of 0.723 eV whereas TEMED treated Li showed an activation energy of 0.48 eV. This decrease in activation energy leads to a much higher mobility of Li^+, which in turn decreases the concentration gradient to provide a more uniform surface for Li^+ migration and plating. To test our hypothesis and to further understand the mechanism for suppression of Lithium (Li) dendrite growth by the Li_3N protective layer, we further characterized the activation energy of Li^+ ion using integrated phase field simulations to elucidate the fundamental correlation between our novel artificial layer with pure phase and the Li^+ ion transport behavior at the interface on both bare and treated Li anodes, which we compare with the experimental results. A highly diffusive SEI layer is introduced on the surface of the Li anode to mimic the treated Li. The diffusivity of

Li-ion in the electrode (D_e) and the electrolyte (D_s) are set to be 3.1×10^{-10} m^2/s and 3.05×10^{-7} m^2/s respectively, while the diffusivity in the artificial SEI layer (D_l) is 6 times larger than D_s. These values are calculated based on the activation energy obtained from experiments (**Figure S2**). Figure 3a, **b** shows snapshots of the Li dendrite structure on bare lithium and lithium having Li_3N as an artificial SEI layer after 300s, respectively. For bare Li, we observe that an initial Li protrude grows into a filament-like dendritic morphology which penetrates the liquid electrolyte. In contrast, the initial Li protrude forms a dome-like morphology in treated lithium. It can thus be inferred that the artificial SEI layer of higher Li-ion diffusivity and higher transference number can significantly suppress the Li dendrite growth from the anode. To further elucidate our findings, we plotted the 1D evolutions of Li-ion concentration along x direction across the tip of the dendrite, as indicated by the arrows in the 2D inset plots (Fig. 3c, **d**). The Li^+ ion concentration at the tip of the dendrite increases sharply for bare lithium, whereas it increases very gradually for treated lithium. This observation supports the convention that bare lithium has a high Li-ion concentration gradient at the dendrite tip that facilitates growth of dendrites.

The electric field variation (E_x) along the dendrite tip at different time steps for both bare lithium and treated lithium are compared in **Fig. 3e, f**. The local electric field remains almost constant in the electrode and electrolyte, but it is maximized at the tip of the dendrite for both the cases. However, for bare lithium, the maximum E_x is 2.5 times that of the treated Li, which is due to the sharper tip morphology with larger curvature, leading to a higher Li-ion concentration gradient near the tip due to the higher local electric field, which further facilitates growth of the dendrite on a bare lithium anode. These results indicates that that Li dendrite growth is a self-accelerating process, agreeing with previous reports[41]. We also observe that for the bare Li E_x at the dendrite tip and $E_x$in the electrolyte solution increases to maximum over time. Whereas, for the treated Li anode, the variation in E_x at different time steps are much less significant, indicating that Li dendrite growth is significantly inhibited.

Elemental analysis, topography and modulus mapping of TEMED treated Li

X-ray photoelectron spectroscopy (XPS) were conducted for both the TEMED treated Li and bare Li to identify and analyze the different types of interactions between the elements and the chemical composition of the TEMED derived protective layer. All the high-resolution spectrums were fitted by the Lorentzian in terms of spin-orbit doublets. Figure 4b shows the high-resolution N 1s spectrum, with peaks at 398.3 eV and 401.5 eV assigned to f Li_3N and LiN_xO_y respectively. Both Li_3N and LiN_xO_y are known to be good Li^+ conductors and can promote efficient and stable cycling of Li metal electrodes. The absence of any peak in Fig. 4e for bare Li confirms that the presence Li_3N and LiN_xO_y arise from the reaction of the TEMED with Li. We believe that this N-rich SEI stabilizes the Li/electrolyte interface, leading to uniform Li electroplating and increased cycle life. Furthermore, we also observed the presence of N from the energy dispersive spectrum (EDS), which shows the distinct presence of N and a uniform distribution of N over the surface of the TEMED treated Li (supplementary information Figure S4).

Atomic force microscopy (AFM) was employed to observe surface topography and measure the corresponding Young's modulus of bare Li and TEMED treated Li as shown in Fig. 4g-j. The surface roughness values of the bare Li and TEMED treated Li were compared by measuring the average surface root mean square (RMS) via high-resolution AFM. The surface topography of bare Li (Fig. 4g) and TEMED treated Li (Fig. 4i) show average RMS roughness values of 242 and 157 nm, respectively. The higher RMS value for bare Li implies uneven and rough surfaces that can create large protuberances on the electrode surface[42]. These protuberances generate non-uniform electric fields during charge/discharge leading to inhomogeneous plating of Li [42, 43]. In contrast, the smooth surface of TEMED treated Li electrode provides a route for uniform Li plating. The corresponding Young's modulus mapping values of bare Li (Fig. 4h) and TEMED treated Li (Fig. 4j) show an average Young's modulus values of 0.32 and 6.85 GPa, respectively. We attribute the 20 times higher Young's modulus value of TEMED treated Li to the superior structural efficiency and mechanical strength of the highly oriented α-phase Li_3N. This Young's modulus value is significantly higher than the threshold value of 6.0 GPa, indicating that the TEMED treated Li electrode can withstand mechanical forces, providing the desired mechanical stability during Li plating/stripping, as well as offering high resistance and sufficient strength to suppress Li dendrite growth[11].

Electrochemical performance of TEMED treated Li

To evaluate the electrochemical performance of the TEMED based lithiophilic interphase, symmetric cells with pristine Li and TEMED treated Li were cycled at various current densities (0.5 mA cm^{-2} and 1 mA cm^{-2}) with the platting/ stripping capacity of 1 mAh cm^{-2} using 1.0 M LiTFSI in 1,3-dioxolane/1,2-dimethoxyethane (DOL/ DME; 1:1) electrolyte. Voltage profile versus cycling time, and voltage hysteresis (estimated by calculating the average difference between the voltage of Li stripping/plating) versus cycle number are shown in Fig. 5.

The plating/stripping voltage profile of bare Li and TEMED treated Li was carried out to investigate interfacial stability of the TEMED-based SEI. Figure 5a,c shows the voltage profile of Li plating/ stripping of bare Li and TEMED treated Li symmetrical cells that achieved a capacity of 1 mAh cm^{-2} at the current density of 0.5 mA cm^{-2} and 1 mA cm^{-2} respectively. At a low current density of 0.5 mA cm^{-2}, bare lithium based symmetric cell exhibited large voltage divergence after 150 cycle, and short circuit after ~ 600 hours. However, TEMED treated lithium based symmetric cell showed a stable voltage profile with hysteresis below 20 mV, reflecting the stable plating and stripping process for more than 3500 hours. Even at the current density of 1 mA cm^{-2}, TEMED treated symmetrical cell showed stable plating and stripping for more than 500 cycles (1000 hours), whereas bare Li metal based symmetrical cell failed after ~ 350 hours. TEMED treated symmetric cell showed stable performance even at a higher current density of 2 mA cm^{-2} (Supplementary Information S6 and S7) and 5 mA cm^{-2} (Supplementary Information S8 – S9). 700 hours and ~ 350 hours have been achieved for 2 mA cm^{-2} and 5 mA cm^{-2} respectively for TEMED treated Li, compared to 150 and 50 hours for bare Li. TEMED treated Li also showed a stable plating and stripping cycle with $LiPF_6$ as an electrolyte (Supplementary Information

S10). The cell showed a stable plating and stripping for more than 750 hours at the current density of 1 mA cm^{-2} for TEMED whereas bare Li failed after 270 hours (Supplementary Information S11). The voltage hysteresis is the difference between the voltages of Li stripping and plating and is mainly determined by the current density, interfacial properties, and charge transfer resistance. For bare Li, an increase in voltage hysteresis was observed with increasing cycles in Fig. 5 **(b)**. The over-potential increases continuously, leading to early failure of the cell after 200 cycles (~ 400 hours). This large hysteresis implies the formation of a highly resistive and unstable interfacial layer. The unstable SEI layer formed during cell operation, consumption of electrolyte to form new SEI layer, and the formation of the dead Li and Li dendrite are reasons for the early failure of the cell[10].

In contrast, TEMED treated Li shows far more stable cycling with stable voltage profiles and constantly low hysteresis over 500 cycles (Fig. 5d), reflecting the stable plating and stripping process with TEMED treated Li electrode in the working cell. The TEMED reacts with the Lithium to form a layer of Lithium nitrate; this Li_3N artificial layer helps to block direct contact between the electrolyte and the Li, which helps stabilize the interface between the Li and the electrolyte. The high mechanical strength of the Li_3N layer also helps suppress formation of Li dendrites because Li^+ can pass easily through the Li_3N layer to deposit underneath. The Li_3N grains also dampen the electric field distribution, leading a uniform Li flux.

To better understand the morphology of Li deposition on bare Li and TEMED treated Li, we analyzed the SEM results after 5, 20 and 100 cycle. Figure 5**(e)** shows a schematic illustration of the growth of Li dendrites and dead Li on the bare Li metal after plating and stripping cycles. For bare Li, native SEI layers from the reaction between the Li and electrolytes are fragile, non-uniform and, unstable. These unstable SEI layers can be easily ruptured by electrode volume changes and by uneven plating/stripping, leading to nucleation sites and inhomogeneous electric fields that accelerate dendritic growth.

In contrast TEMED treated Li (Fig. 5**(f)**) prevents side reactions of Li metal with the electrolyte. We investigated the surface morphology of the TEMED treated Li and bare Li with SEM. Figure 5g-l shows the SEM images of bare Li and TEMED treated Li after 5th, 20th and 100th plating at 0.5 mA cm^{-2} with a capacity of 1 mAh cm^{-2}. For bare Li we observed uneven Li plating and dendrite growth from the 5th cycle (Fig. 5g). The unregulated and unprotected surface of the bare Li creates large protuberances generating a non-uniform electric field, leading to inhomogeneous plating of Li. Dendrite growth is also promoted because of the uneven surface and locally concentrated Li-ion flux because the sharp end of the Li dendrite serves as a center at which charges tend to accumulate.[10, 44]. This needle-like structure with a sharp end may also penetrate through separator to cause an internal short circuit that results in safety issues[45]. Additionally, the surface area associated with the dendritic morphology and side reactions result in an extremely low CE.

In contrast, the TEMED treated Li leads to a dense and nodule-like morphology with no lithium dendrites observed. This compact and nodular artificial layer serves as a physical protection barrier to inhibit penetration of organic electrolyte which could subsequently corrode the underlying Li electrode. Cross sectional SEM (Supplementary Information S15) showed ~ 50µm thickness for the Li case after 100 cycles as compared to ~ 19µm for the TEMED treated sample. Even after 100 cycles of charge/discharge, the surface of TEMED treated Li still maintained a compact surface without distinct dendrites (Fig. 5l). Thus, the compact and uniform artificial layer formed through TEMED serves as an artificial layer that further acts as a barrier to prevent electrolyte from penetrating and corroding the Li electrode. This provides extremely long and stable cycling performance with reduced overpotential. Hence, our structural characterization at a high stripping/plating rate over long cycling times further supports that the high transference number of TEMED treated Li improves the mobility of the Li, which in turn decreases the concentration gradient, leading to uniformity of Li electrodeposition with suppressed lithium dendrite formation.

To evaluate the compatibility of TEMED treated Li as an anode for practical LMBs, we adopted lithium iron phosphate (LFP) and NMC-111 as a cathode to assemble a full cell LMB. Figure 6a shows the cycling performance of the full cell using bare Li or TEMED treated Li as an anode at a constant current density of 1C. We observed linear degradation in capacity for the full cell with bare Li as an anode (Fig. 6a) due to the uneven plating/stripping, Li-dendrite and dead Li. However, in contrast, with the TEMED treated Li as an anode to reduce Li loss efficiently, we obtained a steady and stable capacity for the full cell. In rate capability tests (Fig. 6b), at lower current densities of 0.2C, 0.5C and 1C we observed comparable capacity for bare-Li and TEMED treated Li. However, the transition of the cycles to high current densities of 5C to 0.5C, leads to a large capacity loss for bare Li (Supplementary Information Figure S16 and S17 shows the corresponding charge/discharge voltage profile at different C-rate for bare Li and TEMED treated Li respectively). Unlike bare Li, TEMED-treated Li recovers almost 100% of capacity. This is attributed to the stable dendrite-free Li plating/stripping of the TEMED-treated Li with negligible Li loss due to the highly oriented Li_3N layer that also provides excellent mechanical strength to establish a strong interface and fast ion transfer channel between electrolyte and Li metal. In contrast the bare Li electrode is not able to retain the same capacity as the TEMED treated Li because of the accumulation of SEI and dead Li.

For both for Li/NMC and TEMED-Li/NMC we found that the NMC based full cell during the 5th cycle showed a discharge capacity ~ 123 mAh g^{-1}(Supplementary Information S18). In contrast, for the 100th cycle the specific capacity of bare Li/NMC full cell decrease to ~ 90 mAh g⁻1, whereas TEMED-Li/NMC showed a capacity of ~ 110 mAh g^{-1} (Supplementary Information S17). A drastic decline in capacity for bare Li/NMC with capacity retention of ~ 48% has been obtained as compared to 73% for TEMED-Li/NMC after 200 cycles (Supplementary Information S20) suggesting that the artificial SEI of TEMED treated Li is more stabilized compared to bare Li. Figure 6c,d shows the cycling performance and voltage profile of full cells using both bare Li and TEMED treated Li as an anode. Bare Li/ LFP full cell showed a lower CE in the first cycle, which could be attributed to Li consumption and electrolyte decomposition to form the SEI. During the 10th discharge, the capacity of the TEMED treated Li cell is 140 mAh g^{-1} and it still remains ~ 140 mAh g^{-1} after 100th cycle, retaining ~ 100%. In contrast, the 10th specific discharge capacity of bare Li/LFP full cell shows a sharp decrease from ~ 140 mAh g^{-1} to 102 mAh g^{-1}, retaining

72.8% at the 100th cycle. With increased cycle numbers, the decrease in capacity retention becomes more prominent for bare Li/LFP. During the 200th and 300th cycle discharge we obtained capacities of 86 mAh g^{-1} and 56.3 mAh g^{-1}. Thus degradation in the capacity have been observed with increasing cycles. This degradation in the specific capacitance with the increase in the charge/discharge cycle for bare Li/LFP LMB can be attributed to side reactions and the formation of an unstable and fragile SEI. In contrast, TEMED treated Li/LFP showed a stable discharge capacity even after many cycles. Thus the TEMED stabilized SEI suppresses Li dendrite growth while allowing efficient Li-ion transportation, reducing local current density, decreasing overpotential, and generating homogeneous Li-ion flux distribution[5]. The suppression of Li dendrite growth induces homogeneous Li plating that favors electrolyte compatibility and improves the electrochemical stability, thus leading to long cycles with high specific capacitance[46]. Reduced overpotentials were also observed for the TEMED Li/LFP full cell. In contrast, the bare Li/LFP shows higher overpotential due to the loss of Li and consumption of electrolyte from side reactions and an un-stabilized SEI with dendrites, leading to overpotential and sluggish Li-ion transportation. The stable cycle life and low polarization potential suggest that the **TEMED Li anode is capable of working under practical cycling conditions.**

Discussion

In this work, we demonstrated a facile and efficient solution processed method to provide lithium nitride as a protective layer. The Li_3N-rich SEI successfully suppresses penetration of Li dendrites, while the low electronic conductivity and the intrinsic electrochemical stability of Li_3N block side reactions between the electrolyte and Li. This artificial SEI layer offers excellent Li^+ ion conductivity with lower Li^+ ions migration energy barriers that further benefit ion transport at the interface between the electrode and electrolyte. This can effectively facilitate the transport of Li^+ ions across the electrode surface leading to high transference number, and excellent mechanical strength which results in more uniform Li^+ ion flux.

Here, we showed that the liquid electrolytes increase their cation transference number (from 0.37 to 0.66) when confined to a structurally rigid Li_3N host. This enabled a stable interface between the lithium and electrolyte that suppresses Li dendrite formation. With effective suppression of dendrite growth, TEMED treated Li electrode display significantly longer Li plating/stripping cycles and reduced overpotential. As a result, we demonstrated long stable plating/stripping cycling up-to 3500 hours at 0.5 mA cm^{-2} along with a full cell cycling up-to 500 cycle at 1C rate. These dendrite free TEMED treated Li should facilitate applications of high energy density Li metal batteries.

Methods

Materials and synthesis

Li chips (diameter size = 15.6 mm and thickness = 450 µm) were purchased from MTI Corp. Tetramethylethylenediamine (TEMED) was purchased from Sigma Aldrich. TEMED was used without any further modifications.

Lithium chips were allowed to be completely immersed into the TEMED in the petri dish and was kept overnight. The Li chips were allowed to be dried at 60°C for half an hour to let the unreacted liquid to evaporate away. The dried Li chips were then used for the further analysis and cell fabrications.

Electrode Fabrication

Lithium iron phosphate (LFP) powders were mixed with Super-P carbon black and polyvinylidene fluoride (PVDF) at a weight ratio of 80:10:10, respectively, in the *N*-methyl-2-pyrrolidone (NMP) solvent to form a slurry using the mortar and pestle. The slurry was coated on an aluminum foil current collector by doctor blading and then dried in the vacuum oven at 80°C for 12 hours. The dried samples were cut into circular disks with a diameter of 12 mm and used as the working electrode. The total areal mass loading of the NMC electrode was ≈ 2.5 mg cm^{-2} and the areal mass loading of active material LTO was ≈ 2.0 mg cm^{-2}

Electrochemical Characterization

The CR-2032 Li-ion coin cell was assembled inside an argon-filled glove box (moisture and O2 level < 0.1 ppm) for all the electrochemical measurements. Celgard 2500 with a film thickness of 25 μm was used as a separator, and the electrolyte was 1M Lithium bis(trifluoromethanesulfonyl)imide (LiTFSI, Sigma Aldrich) in 1,3-dioxolane (DOL, Sigma Aldrich)/ 1, 2-dimethoxyethane (DME) Sigma Aldrich) (1:1 volume ratio) with 1 wt% Li nitrate (LiNO3, Alfa Aesar). The amount of electrolyte used was controlled as ~ 60 uL for each cell. Cells were tested under a different current density of 0.5 and 1 mA cm^{-2} with the capacity of 1 mAh cm^{-2} using Land battery analyzer (CT2001A). Li/LFP cells were cycled at the voltage range between 2.5 and 4.2 V at 1C.

Electrochemical impedance spectroscopy (EIS) was carried out by a Biologic VSP potentiostat with frequency ranging from 0.1Hz to 100K Hz. XRD of the samples was conducted on a Rigaku SmartLab diffractometer with Cu Kα radiation (λ = 1.54178 Å). Topography and Young's Modulus of bare Li and graphite–SiO2 Li were measured using an Agilent SPM 5500 atomic force microscope equipped with a MAC III controller using a tip (product RTESPA-525) with the resonance frequency of 75 kHz. Raman spectroscopy was carried out using the Horiba Raman system with 532 nm laser.

SEM characterization was carried out using a Hitachi S-4300N SEM. Galvanostatic charge–discharge measurements of the coin cells were carried out using the LAND CT2001A system.

Phase-field simulation

The phase field simulations were performed on COMSOL. The Multiphysics software used general PDE and the solver was set as time-dependent. The size of the model is chosen to be 500×500 μm^2. Dirichlet boundary conditions were selected for the Nernst-Planck equation (Eq. 2 Supplementary Information) and the current continuity equation (Eq. 3 Supplementary Information), while the zero-flux boundary condition is set for the phase-field variable (ξ). C_{Li} is fixed at 1.0 mol/L in the electrolyte and 0.0 mol/L in the electrode, while φ is fixed at -0.35 V in the electrode and 0.0V in the electrolyte as the boundary conditions. The initial state is a pure electrolyte, in which ξ and φ are set to be zero, while the initial value for C_{Li} is set to be 1.0 mol/L. Then, a semi-circle type random noise is added on the surface of the Li anode, which acts as a nucleus for Li dendrite growth. The diffusivity of Li-ion is set to be D^s = 3.05×10^{-7} m^2/s in the electrolyte solution, and D^e = 3.1×10^{-10} m^2/s in the Li electrode, based on the activation energy of bare Li from experimental measurement. To study the effect of the Li_3N protective layer on the Li deposition morphology, we introduced a high diffusive SEI layer on the surface of the Li anode to mimic the treated Li. The diffusivity of this layer (D^i) is 6 times of D^s, based on the activation energy of treated Li from experimental measurement.

Declarations

Acknowledgments

This work is supported by the National Science Foundation under awards CBET- 2038082, CBET-2038083, and OIA-2132021. AC and KX thank the support from Joint Center of Energy Storage Research, an Energy Hub funded by US Department of Energy Basic Energy Science. We also acknowledge the support from South Dakota Governor’s Research Center, SDBoR Competitive Grant Program, and EDA University Center Program (ED18DEN3030025).

Author information

Authors and Affiliations

Department of Electrical Engineering and Computer Science, South Dakota State University, Brookings, SD 57007, USA

Jyotshna Pokharel, Ashim Gurung, Wei He, Abiral Baniya, Buddhi Sagar Lamsal & Yue Zhou

Battery Science Branch, Energy Science Division, U.S. CCDC Army Research Laboratory, Adelphi, MD, 20783, USA

Arthur Cresce & Kang Xu

Department of Materials Science and Engineering, University of Texas at Arlington, Arlington, TX, 76019, USA

Bharat Pant & Ye Cao

Department of Mechanical Engineering, South Dakota State University, Brookings, SD 57007, USA

Stephen Gent

Materials and Process Simulation Center, California Institute of Technology, Pasadena, California 91125, USA

William A. Goddard

Contributions

J.P. conceived and led the project. J.P. and A.G. designed the project and experiments. A.C. performed XPS characterization. B.P. and Y.C. performed phase field simulation and analysis. W. H., A.B. Z.Y. and B.S.L. assisted in material characterization and participated in performing ex-situ SEM experiments. S.G. reviewed the paper. Y.C., W.A.G., K.X. and Y.Z. analyzed the overall results and supervised the work. J.P. wrote the paper with assistance from coauthors. All authors have discussed the paper.

Corresponding authors

Correspondence to Ye Cao, William A. Goddard, Kang Xu or Yue Zhou.

References

1. Bruce PG, Freunberger SA, Hardwick LJ, Tarascon J-M. Li–O 2 and Li–S batteries with high energy storage. Nature materials **11**, 19–29 (2012).
2. Ye H, Xin S, Yin Y-X, Li J-Y, Guo Y-G, Wan L-J. Stable Li plating/stripping electrochemistry realized by a hybrid Li reservoir in spherical carbon granules with 3D conducting skeletons. Journal of the American Chemical Society **139**, 5916–5922 (2017).
3. Goodenough JB, Kim Y. Challenges for rechargeable Li batteries. Chemistry of materials **22**, 587–603 (2010).
4. Schmuch R, Wagner R, Hörpel G, Placke T, Winter M. Performance and cost of materials for lithium-based rechargeable automotive batteries. Nature Energy **3**, 267–278 (2018).
5. Lin D, Liu Y, Cui Y. Reviving the lithium metal anode for high-energy batteries. Nature nanotechnology **12**, 194 (2017).
6. Tarascon J-M, Armand M. Issues and challenges facing rechargeable lithium batteries. In: *Materials for sustainable energy: a collection of peer-reviewed research and review articles from Nature Publishing Group*). World Scientific (2011).
7. Xu W, *et al.* Lithium metal anodes for rechargeable batteries. Energy & Environmental Science **7**, 513–537 (2014).
8. Pathak R, *et al.* Fluorinated hybrid solid-electrolyte-interphase for dendrite-free lithium deposition. Nature communications **11**, 1–10 (2020).

9. Gurung A, *et al.* A review on strategies addressing interface incompatibilities in inorganic all-solid-state lithium batteries. Sustainable Energy & Fuels **3**, 3279–3309 (2019).
10. Chen K, *et al.* Flower-shaped lithium nitride as a protective layer via facile plasma activation for stable lithium metal anodes. Energy Storage Materials **18**, 389–396 (2019).
11. Pathak R, *et al.* Ultrathin bilayer of graphite/SiO2 as solid interface for reviving Li metal anode. Advanced Energy Materials **9**, 1901486 (2019).
12. Li NW, Yin YX, Yang CP, Guo YG. An artificial solid electrolyte interphase layer for stable lithium metal anodes. Advanced materials **28**, 1853–1858 (2016).
13. Lang J, *et al.* One-pot solution coating of high quality LiF layer to stabilize Li metal anode. Energy Storage Materials **16**, 85–90 (2019).
14. Fan L, Zhuang HL, Gao L, Lu Y, Archer LA. Regulating Li deposition at artificial solid electrolyte interphases. Journal of Materials Chemistry A **5**, 3483–3492 (2017).
15. Zhu J, *et al.* Rational design of graphitic-inorganic Bi-layer artificial SEI for stable lithium metal anode. Energy Storage Materials **16**, 426–433 (2019).
16. Wang G, *et al.* Suppressing dendrite growth by a functional electrolyte additive for robust Li metal anodes. Energy Storage Materials **23**, 701–706 (2019).
17. Wang D, *et al.* A long-lasting dual-function electrolyte additive for stable lithium metal batteries. Nano Energy, 104889 (2020).
18. Park S-J, Hwang J-Y, Sun Y-K. Trimethylsilyl azide (C 3 H 9 N 3 Si): a highly efficient additive for tailoring fluoroethylene carbonate (FEC) based electrolytes for Li-metal batteries. Journal of Materials Chemistry A **7**, 13441–13448 (2019).
19. Zheng J, *et al.* Electrolyte additive enabled fast charging and stable cycling lithium metal batteries. Nature Energy **2**, 1–8 (2017).
20. Ma Y, *et al.* Enabling reliable lithium metal batteries by a bifunctional anionic electrolyte additive. Energy Storage Materials **11**, 197–204 (2018).
21. Lu Y, Tu Z, Archer LA. Stable lithium electrodeposition in liquid and nanoporous solid electrolytes. Nature materials **13**, 961–969 (2014).
22. Chen K, *et al.* A copper-clad lithiophilic current collector for dendrite-free lithium metal anodes. Journal of Materials Chemistry A **8**, 1911–1919 (2020).
23. Lin D, *et al.* Layered reduced graphene oxide with nanoscale interlayer gaps as a stable host for lithium metal anodes. Nature nanotechnology **11**, 626–632 (2016).
24. Liu Y, Lin D, Liang Z, Zhao J, Yan K, Cui Y. Lithium-coated polymeric matrix as a minimum volume-change and dendrite-free lithium metal anode. Nature communications **7**, 10992 (2016).
25. Jin C, *et al.* 3D lithium metal embedded within lithiophilic porous matrix for stable lithium metal batteries. Nano Energy **37**, 177–186 (2017).
26. Wang Y, *et al.* Polyethylene separators modified by ultrathin hybrid films enhancing lithium ion transport performance and Li-metal anode stability. Electrochimica Acta **259**, 386–394 (2018).

27. Pan R, *et al.* Nanocellulose modified polyethylene separators for lithium metal batteries. Small **14**, 1704371 (2018).
28. Liu Y, *et al.* Dendrite-free lithium metal anode enabled by separator engineering via uniform loading of lithiophilic nucleation sites. Energy Storage Materials **19**, 24–30 (2019).
29. Li G, *et al.* Stable metal battery anodes enabled by polyethylenimine sponge hosts by way of electrokinetic effects. Nature Energy **3**, 1076–1083 (2018).
30. Sand HJ. On the concentration at the electrodes in a solution, with special reference to the liberation of hydrogen by electrolysis of a mixture of copper sulphate and sulphuric acid. *Proceedings of the Physical Society of London (1874*–1925) **17**, 496 (1899).
31. Chazalviel J-N. Electrochemical aspects of the generation of ramified metallic electrodeposits. Physical review A **42**, 7355 (1990).
32. Fang Y, Zhang SL, Wu Z-P, Luan D, Lou XWD. A highly stable lithium metal anode enabled by Ag nanoparticle–embedded nitrogen-doped carbon macroporous fibers. Science Advances **7**, eabg3626 (2021).
33. Gao M, *et al.* Lithium metal batteries for high energy density: fundamental electrochemistry and challenges. Journal of Energy Chemistry, (2020).
34. Diederichsen KM, McShane EJ, McCloskey BD. Promising routes to a high Li + transference number electrolyte for lithium ion batteries. ACS Energy Letters **2**, 2563–2575 (2017).
35. Fong KD, Self J, Diederichsen KM, Wood BM, McCloskey BD, Persson KA. Ion transport and the true transference number in nonaqueous polyelectrolyte solutions for lithium ion batteries. ACS central science **5**, 1250–1260 (2019).
36. Shim J, Kim HJ, Kim BG, Kim YS, Kim D-G, Lee J-C. 2D boron nitride nanoflakes as a multifunctional additive in gel polymer electrolytes for safe, long cycle life and high rate lithium metal batteries. Energy & Environmental Science **10**, 1911–1916 (2017).
37. Wood III DL, Li J, Daniel C. Prospects for reducing the processing cost of lithium ion batteries. Journal of Power Sources **275**, 234–242 (2015).
38. Zhang W, Zhuang HL, Fan L, Gao L, Lu Y. A “cation-anion regulation” synergistic anode host for dendrite-free lithium metal batteries. Science advances **4**, eaar4410 (2018).
39. Li W, *et al.* Li + ion conductivity and diffusion mechanism in a-Li3N and b-Li3N.
40. Zhao J, Wang L, He X, Wan C, Jiang C. Determination of lithium-ion transference numbers in LiPF6–PC solutions based on electrochemical polarization and NMR measurements. Journal of The Electrochemical Society **155**, A292 (2008).
41. Cheng Q, *et al.* Operando and three-dimensional visualization of anion depletion and lithium growth by stimulated Raman scattering microscopy. Nature communications **9**, 1–10 (2018).
42. Guan X, *et al.* Controlling nucleation in lithium metal anodes. Small **14**, 1801423 (2018).
43. Xiang J, *et al.* Improved rechargeability of lithium metal anode via controlling lithium-ion flux. Advanced Energy Materials **8**, 1802352 (2018).

44. Park K, Goodenough JB. Dendrite-Suppressed Lithium Plating from a Liquid Electrolyte via Wetting of Li3N. Advanced Energy Materials **7**, 1700732 (2017).
45. Miao R, Yang J, Xu Z, Wang J, Nuli Y, Sun L. A new ether-based electrolyte for dendrite-free lithium-metal based rechargeable batteries. Scientific reports **6**, 1–9 (2016).
46. Li X, *et al.* An ultrafast rechargeable lithium metal battery. Journal of Materials Chemistry A **6**, 15517–15522 (2018).

Figures

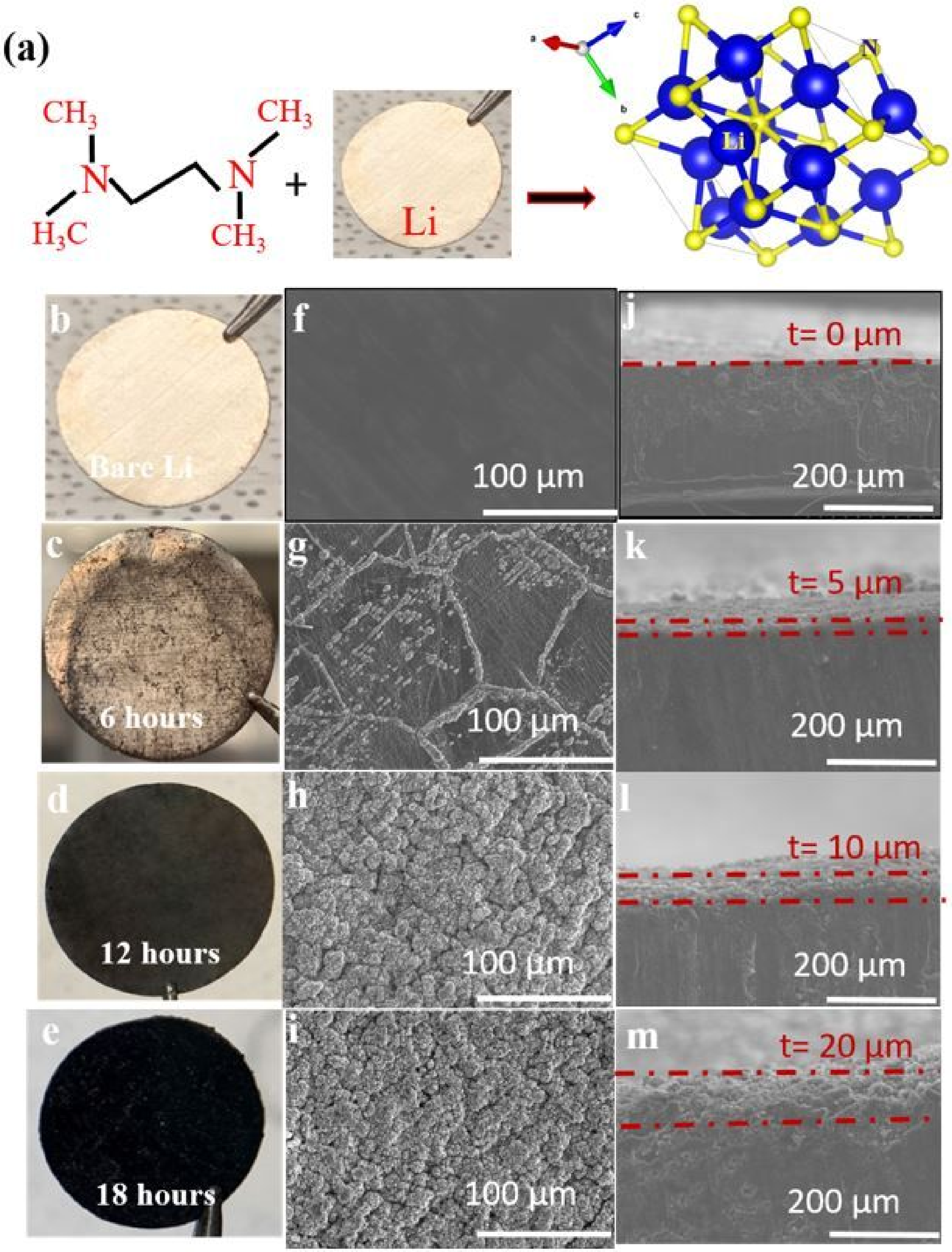

Figure 1

Schematic for reaction of TEMED with lithium metal to produce lithium nitride **(a).** Photographic images of Li treated with TEMED for different treatment times **b-e**. The corresponding cross-sectional SEM images **f-i**. Corresponding top-view SEM images **j-m**.

Figure 2

Contact angle measurement of (a) bare Li, (b) TEMED treated Li, (c) XRD spectrum for TEMED treated Li. (d) EIS measurement for bare Li and TEMED treated Li. Steady-state current under 10 mV polarization for (e) Li-Li symmetric cell (f) TEMED-Li/TEMED-Li symmetric cell. Inset shows EIS measurement before and after polarization.

Figure 3

Phase-field simulation of Li dendrite growth from bare Li anode and from Li anode covered with Li_3N protective layer of high Li ion diffusivity. (a) Dendrite morphology grown on bare lithium metal represented by phase-field variable ξ. (b) Dendrite morphology grown on lithium metal having high diffusivity protective layer made of Li_3N. (c) Concentration profile of Li^+ ion across the x-axis along the tip of the dendrite for bare lithium. The image on the inset shows the concentration of Li^+ ion across the battery. (d) Li^+ ion concentration profile along the tip of dendrite for lithium having high diffusivity Li_3N layer. (e) Electric field profile along the tip of dendrite for bare lithium. The image on the inset shows the 2D distribution of the electric field. (f) Electric field profile along the tip of the dendrite for lithium having high diffusive Li_3N layer.

Figure 4

XPS L1s spectra for TEMED treated Li **(a)** and Bare Li **(b)**, N1s spectra for TEMED treated Li **(c)** and Bare Li **(d)** and O1s spectra for TEMED treated Li **(e)** and Bare Li **(f)**. AFM topography and Young’s modulus mapping (g) (h), TEMED treated Li topography and Young’s modulus mapping (i) and (j).

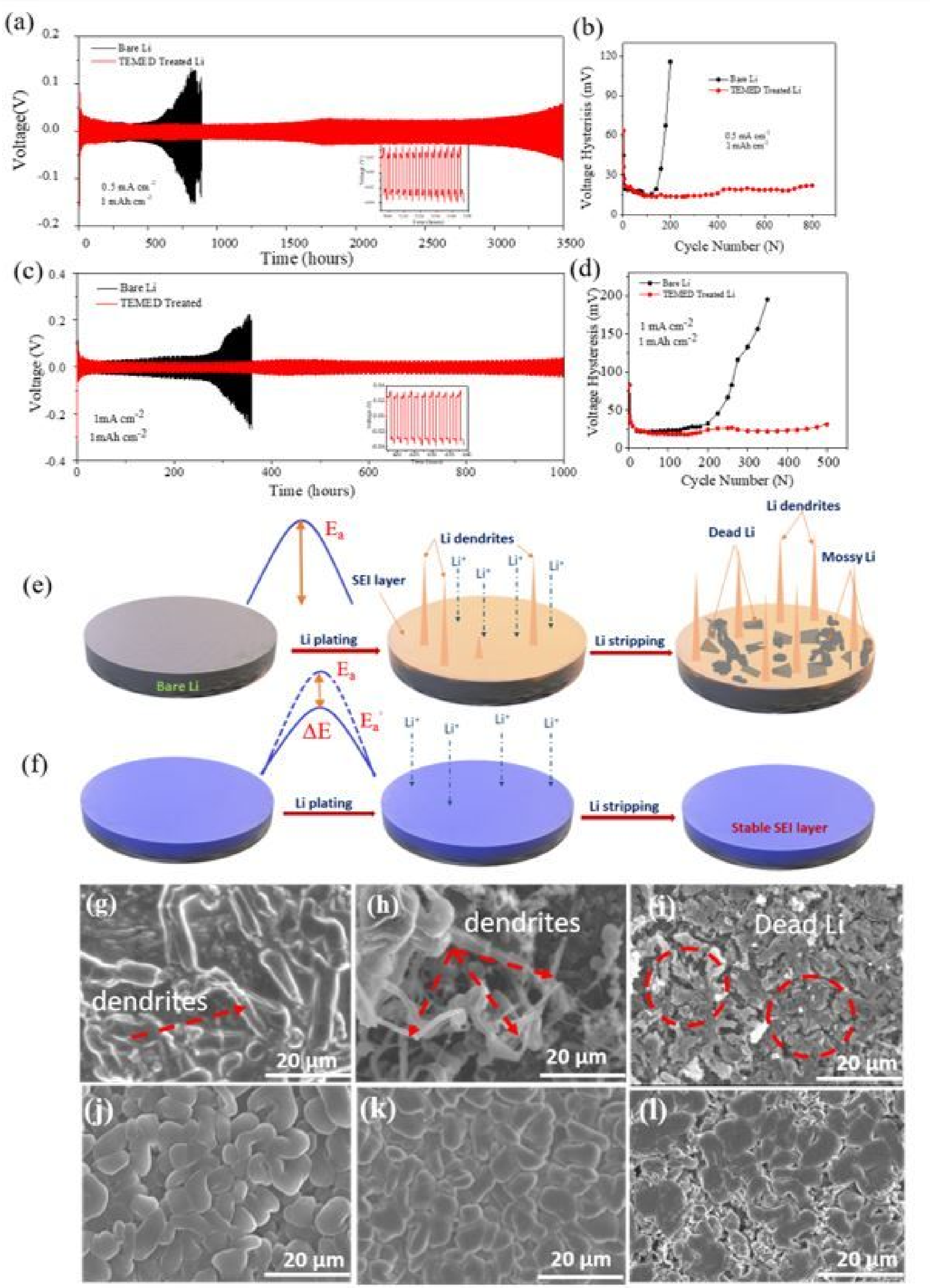

Figure 5

Long term cycling of symmetrical cells at the current density of 0.5 mA cm^{-2} **(a)** and voltage hysteresis at 0.5 mA cm^{-2} **(b).** Long term cycling of symmetrical cells at the current density of 1 mA cm^{-2} **(c)** and Voltage hysteresis at1 mA cm^{-2}(d). Schematic illustration of Li dendrite growth on bare Li (e) and uniform deposition on TEMED treated artificial SEI layered Li (f). SEM image of bare Li (g) (h), (i) and TEMED treated Li (j), (k) and (l) at 5th, 20th and 100th plating respectively. The scale bars are at 20 μm.

Figure 6

(a) Long-term cycling performance of batteries at a current density of 1C. **b**. Rate capability comparison of LFP coupled with bare Li and TEMED treated Li. **c,d** Charge/discharge voltage profiles at different cycle for LFP coupled with bare Li and TEMED treated Li at 1C.

Supplementary Files

This is a list of supplementary files associated with this preprint. Click to download.

- SupportingInformation.docx